

Transformation Optics Approach to Plasmon-Exciton Strong Coupling in Nanocavities

Rui-Qi Li,^{1,2} D. Hernandez-Perez,¹ F. J. Garcıa-Vidal,^{1,3,†} and A. I. Fernandez-Domınguez^{1,*}

¹*Departamento de Fısica Teorica de la Materia Condensada and Condensed Matter Physics Center (IFIMAC), Universidad Autonoma de Madrid, E-28049 Madrid, Spain*

²*Key Laboratory of Modern Acoustics, MOE, Institute of Acoustics, Department of Physics, Nanjing University, Nanjing 210093, People's Republic of China*

³*Donostia International Physics Center (DIPC), E-20018 Donostia/San Sebastian, Spain*

(Received 30 May 2016; published 30 August 2016)

We investigate the conditions yielding plasmon-exciton strong coupling at the single emitter level in the gap between two metal nanoparticles. Inspired by transformation optics ideas, a quasianalytical approach is developed that makes possible a thorough exploration of this hybrid system incorporating the full richness of its plasmonic spectrum. This allows us to reveal that by placing the emitter away from the cavity center, its coupling to multipolar dark modes of both even and odd parity increases remarkably. This way, reversible dynamics in the population of the quantum emitter takes place in feasible implementations of this archetypal nanocavity.

DOI: 10.1103/PhysRevLett.117.107401

Plasmon-exciton-polaritons (PEPs) are hybrid light-matter states that emerge from the electromagnetic (EM) interaction between surface plasmons (SPs) and nearby quantum emitters (QEs) [1,2]. Crucially, PEPs only exist when these two subsystems are strongly coupled; i.e., they exchange EM energy coherently in a time scale much shorter than their characteristic lifetimes. Recently, much attention has focused on PEPs, since they combine the exceptional light concentration ability of SPs with the extreme optical nonlinearity of QEs. These two attributes makes them promising platforms for the next generation of quantum nanophotonic components [3].

A quantum electrodynamics description of plasmonic strong coupling of a single QE has been developed for a flat metal surface [4], and isolated [5,6] and distant nanoparticles [7–9], where SP hybridization is not fully exploited. From the experimental side, in recent years, PEPs have been reported in emitter ensembles [10–13], in which excitonic nonlinearities are negligible [14–16]. Only very recently, thanks to advances in the fabrication and characterization of large Purcell enhancement nanocavities [17–19], far-field signatures of plasmon-exciton strong coupling for single molecules have been reported experimentally [20].

In this Letter, we investigate the plasmonic coupling of a single emitter in a paradigmatic cavity, thoroughly explored in the context of optical antennas thanks to its ability to confine EM fields at very deep subwavelength scales: the nanometric gap between two spherical-shaped metal particles [13,19,20]. We develop a quasianalytical approach that fully exploits the covariance of Maxwell equations and is based on the method of inversion [21]. Inspired by recent advances in transformation optics (TO) [22,23], this approach fully accounts for the rich EM spectrum that originates from SP hybridization across the gap.

Our theory, which is the first application of the TO framework for the description of quantum optical phenomena, yields quasianalytical insight into the Wigner-Weisskopf problem [24] for these systems, and enables us to reveal the prescriptions that nanocavities must fulfil to support single QE PEPs.

Figure 1(a) sketches the system under study: a two level system (with transition frequency ω_E and z -oriented dipole moment μ_E) placed at position z_E within the gap δ between two spheres of permittivity $\epsilon(\omega) = \epsilon_\infty - [\omega_p^2/\omega(\omega + i\gamma)]$, embedded in a matrix of dielectric constant ϵ_D [see Supplemental Material (SM) [25] for further details]. We assume that the structure is much smaller than the emission wavelength and operate within the quasistatic approximation. The details of our treatment of SP-QE coupling in this geometry can be found in the SM. Briefly, by inverting the structure with respect to a judiciously chosen point [z_0 in Figure 1(a)], the spheres map into an annulus geometry in which the QE source and scattered EM fields are expanded in terms of the angular momentum l . This allows us to obtain the scattering Green's function, $G_{zz}^{sc}(\omega)$, in a quasianalytical fashion.

First we test our approach by analyzing the spontaneous emission enhancement experienced by an emitter at the gap center. Figure 1(b) plots the Purcell factor $P(\omega) = 1 + (6\pi c/\omega)\text{Im}\{G_{zz}^{sc}(\omega)\}$ for dimers with $R_{1,2} = R$. To compare different sizes, $P(\omega)$ is normalized to R^{-3} . Black solid line plots the TO prediction (identical for all sizes), and color dots render full EM calculations (Comsol *Multiphysics*). At high frequencies, quasianalytics and simulations are in excellent agreement for all R . At low frequencies, discrepancies caused by radiation effects are evident for $R \gtrsim 30$ nm. The insets in Figure 1(b) render induced charge density maps for the four lowest peaks in

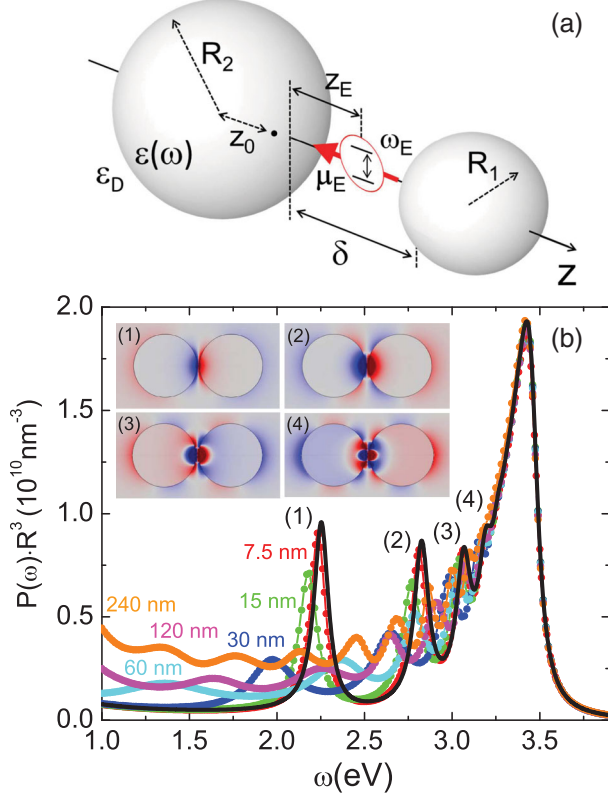


FIG. 1. (a) QE placed at the gap between two metal spheres of permittivity $\epsilon(\omega)$ and embedded in a dielectric medium ϵ_D . The QE dipole strength, position, and frequency are μ_E , z_E , and ω_E . (b) Normalized Purcell factor at the gap center for $R_{1,2} = R$ and $\delta = R/15$. Color dots: EM simulations for different R . Black line: TO prediction. Insets: induced charge distribution for the lowest 4 SP modes discernible in the spectrum (color scale is saturated for clarity).

the TO spectrum. These can be identified as SP resonances of increasing multipolar order. We can infer that the maximum that dominates all the spectra in Figure 1(b) is caused by the pseudomode (ω_{PS}) emerging from the spectral overlapping of higher order SPs [16]. Importantly, these are darker (weakly radiative) modes strongly confined at the gap region, which explains why our quasistatic description is valid at ω_{PS} even for $R = 240 \text{ nm}$.

Now we investigate the spectral density across the gap cavity. This magnitude governs SP-QE interactions (see below), and can be expressed as $J(\omega) = (\mu_E^2 \omega^3 / 6\pi^2 \epsilon_0 \hbar c^3) P(\omega)$. Figure 2(a) shows TO- $J(\omega)$ evaluated at $z_E = \delta/2$ and normalized to μ_E^2 / R^3 for different δ/R . For small gaps, the spectral density is maximized, and the contribution from different SPs is apparent. For larger gaps, $J(\omega)$ decreases, all maxima blue-shift and eventually merge at the pseudomode position. Importantly, Fig. 2(a) shows a universal trend, valid for all QEs and R (within the quasistatic approximation). Therefore, for a given δ/R , large μ_E and small R must be used to increase plasmon-exciton coupling.

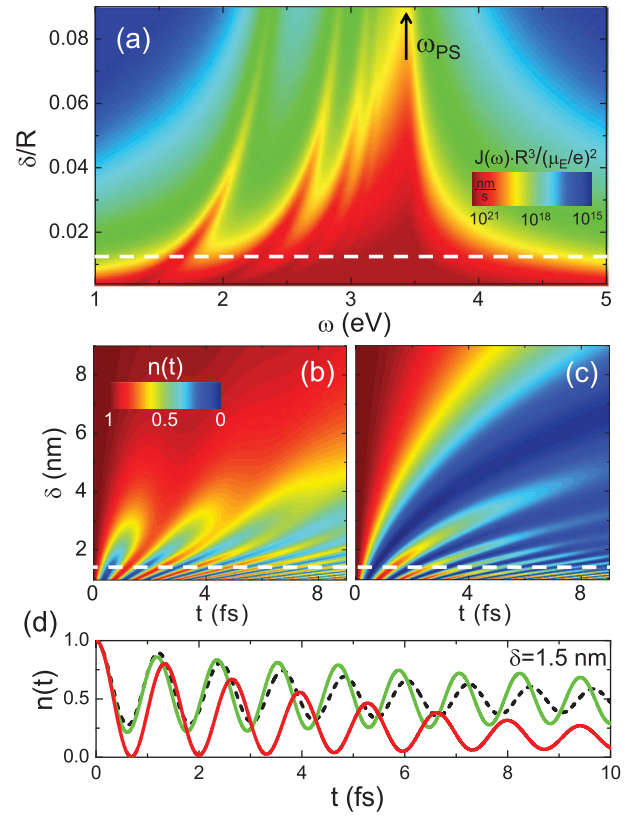


FIG. 2. (a) Normalized $J(\omega)$ at the gap center versus frequency and δ/R . (b),(c) $n(t)$ versus time and gap size for $R = 120 \text{ nm}$ and $\mu_E = 1.5 e \text{ nm}$. The QE is at resonance with the lowest (dipolar) SP mode in (b) and with the pseudomode in (c). (d) $n(t)$ for $\delta = 1.5 \text{ nm}$ (see white dashed lines) and two ω_E : 1.7 (green) and 3.4 (red) eV. Black dotted line corresponds to $\omega_E = 1.7 \text{ eV}$ obtained through the fitting of $J(\omega)$ at ω_{PS} .

Once the spectral density is known, the Wigner-Weisskopf problem [24] can be solved. It establishes that the equation governing the dynamics of the excited-state population, $n(t) = |c(t)|^2$, for an initially excited QE is

$$\frac{d}{dt} c(t) = - \int_0^t d\tau \int_0^\infty d\omega J(\omega) e^{i(\omega_E - \omega)(t - \tau)} c(\tau). \quad (1)$$

Figures 2(b) and 2(c) render the QE population at the center of the cavity in panel (a) as a function of time and gap size. The spheres radius is 120 nm (so that $1 \lesssim \delta \lesssim 10 \text{ nm}$), and $\mu_E = 1.5 e \text{ nm}$ (InGaN/GaN quantum dots at 3 eV [30]). The emitter is at resonance with the lowest (dipolar) SP (b) and with the pseudomode (c) maxima in Fig. 2(a), respectively. Note that the former disperses with gap size, whereas $\omega_E = \omega_{PS}$ for the latter. We can observe that both configurations show clear oscillations in $n(t)$, which indicates that coherent energy exchange is taking place. In this regime, strong coupling occurs, and the nanocavity supports PEPs. However, for $\delta > 3 \text{ nm}$, the reversible dynamics in the population is lost in both panels; QEs

and SPs are only weakly coupled, and $n(t)$ follows a monotonic decay.

Figure 2(d) plots $n(t)$ at strong coupling, $\delta = R/80 = 1.5$ nm [see white dashed lines in panels (a)–(c)]. The red (green) line corresponds to QE at resonance with the pseudomode (dipolar SP) peak. The excited state population obtained from the fitting of $J(\omega)$ around ω_{PS} and evaluated at the lowest SP frequency is shown as a black dashed line. The similarity between solid green and dashed black lines implies that the population dynamics is fully governed by the pseudomode, even when the two maxima in $J(\omega)$ are far apart [the differences between Figs. 2(b) and 2(c) originate from detuning effects]. This fact enables us to extend the validity of our approach to larger structures, as radiative effects do not play a significant role at the pseudomode. More importantly, our findings reveal that QE strong coupling in nanocavities does not benefit from highly radiative plasmonic modes despite their low resonant frequencies and associated low sensitivity to metal absorption.

We have found that $R = 120$ nm cavities can support single QE PEPs only if $\delta < 4$ nm. Similar calculations for single particles (not shown here) indicate that the onset of strong coupling takes place at similar distances, $z_E \lesssim 2$ nm. This means that the configuration investigated so far does not exploit cooperative effects between the nanospheres, associated with the enhancement in $J(\omega)$ expected from SP hybridization. To verify this, Fig. 3(a) plots $J(\omega_{PS})$ versus δ evaluated at the center of the cavity and normalized to twice the maximum in the spectral density for an isolated sphere ($R = 120$ nm, $z_E = \delta/2$). Whereas normalized $J(\omega_{PS})$ is much larger than 1 for $\delta = 1.5$ nm, it decays to ~ 0.5 for gaps larger than 4 nm. Therefore, only very small gap cavities take advantage of SP hybridization. The inset of Fig. 3(a) plots $J(\omega)$ for 120 nm radius dimer (blue) and single sphere (green) evaluated at $z_E = 4$ nm, showing that the maximum spectral density is very similar in both cases.

We explore next the effect that moving the QE away from the gap center has on the cavity performance. We consider $\delta = 8$ nm, for which strong coupling does not take place at $z_E = \delta/2$; see Figs. 2(b) and 2(c). Figure 3(b) plots $J(\omega_{PS})$ versus z_E for two different normalizations. Black dashed line shows the ratio of $J(\omega_{PS})$ and its value at $z_E = \delta/2$. We can observe that the spectral density maximum grows exponentially as the QE approaches one of the particles, yielding factors up to 10^3 . This effect could be attributed to the stronger interaction with the SPs supported by the closest sphere. To test this, red solid line plots $J(\omega_{PS})$ now normalized to the sum of the spectral densities calculated for each of the spheres isolated and evaluated at z_E and $\delta - z_E$. Remarkably, enhancements up to 10^2 are found in this asymmetric configuration. Therefore, the pronounced increase of $J(\omega)$ cannot be simply caused by proximity effects, but it must be due to a significant enhancement of the cooperativity between the two nanoparticles. Figure 3(c) plots $n(t)$ for three z_E values

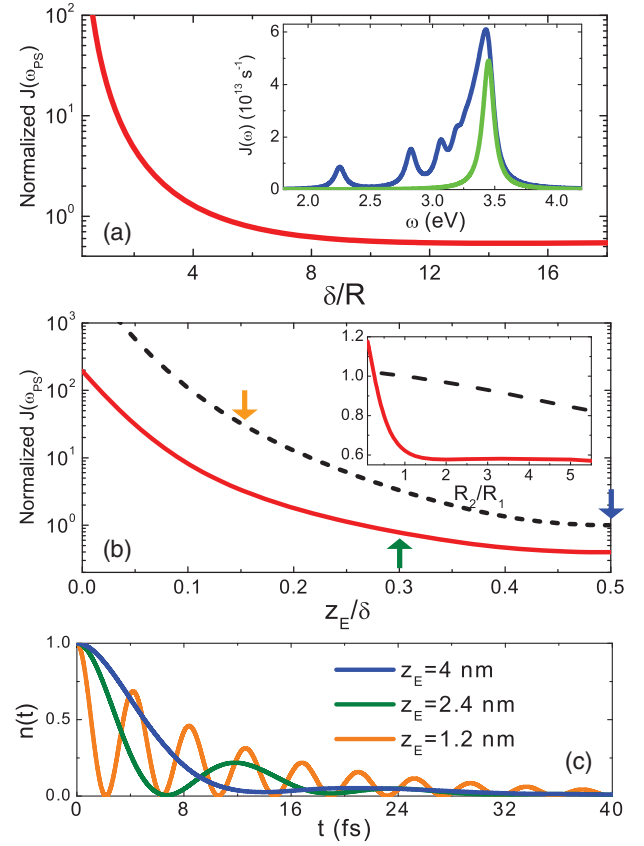


FIG. 3. (a) $J(\omega)$ at $z_E = \delta/2$ and $\omega_E = \omega_{PS}$ versus δ normalized to the sum of the spectral density maxima for the spheres isolated. Inset: $J(\omega)$ for the dimer (blue) and isolated particle (green) for $\delta = 8$ nm, $R = 120$ nm. (b) Spectral density at the pseudomode versus z_E/δ . Red solid line: $J(\omega_{PS})$ normalized to the sum of the two spheres isolated. Black dashed line: $J(\omega_{PS})$ normalized to its value at $z_E = \delta/2$. Inset: Same but versus the ratio R_2/R_1 for $z_E = \delta/2$. (c) $n(t)$ for $\omega_E = \omega_{PS}$ and three z_E values ($\mu_E = 1.5$ e nm).

[indicated by vertical arrows in panel (b)], proving that strong coupling occurs for z_E far from the cavity center. The inset of Fig. 3(b) investigates if SP-QE coupling can benefit further from geometric asymmetry. It renders $J(\omega_{PS})$ versus R_2/R_1 for both normalizations, and proves that the cavity performance is rather independent of the particle sizes in the regime $R_{1,2} \gg \delta$.

To gain physical insight into the dependence of $J(\omega)$ on the QE position, we assume that $\delta \ll R_{1,2}$, and work within the high quality resonator limit [6]. This way, we can obtain analytical expressions for $J(\omega)$, which can be written as a sum of Lorentzian SP contributions of the form

$$J(\omega) = \sum_{l=0}^{\infty} \sum_{\sigma=\pm 1} \frac{g_{l,\sigma}^2}{\pi} \frac{\gamma/2}{(\omega - \omega_{l,\sigma})^2 + (\gamma/2)^2}, \quad (2)$$

where the index l can be linked to the multipolar order of the SP, σ to its even (+1) or odd (−1) character, and γ is the damping parameter in $\epsilon(\omega)$.

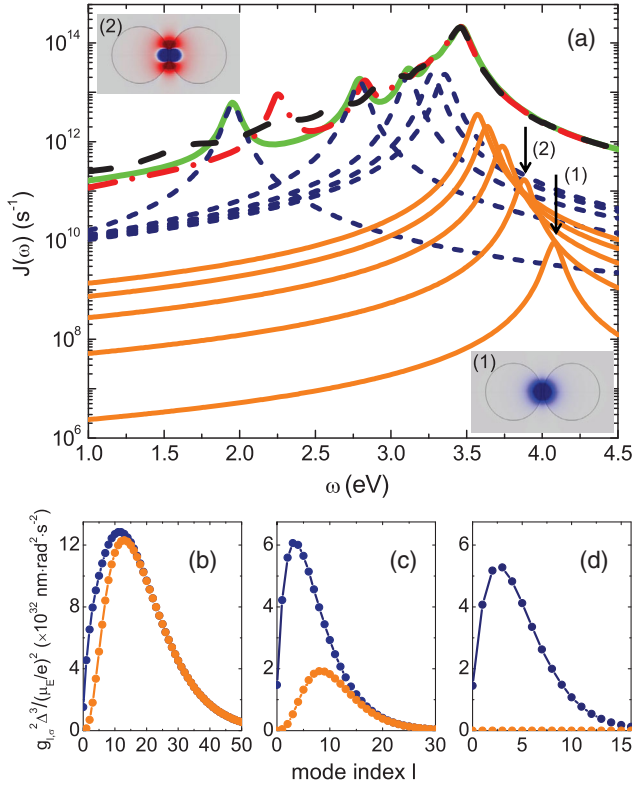


FIG. 4. (a) Spectral density for $z_E = 2.4$ nm obtained through numerical (black dashed line), exact TO (red dotted-dashed line), and analytical TO (solid green line) calculations. The contribution to $J(\omega)$ due to even and odd modes are plotted in dark blue dotted and solid orange lines, respectively. Inset: surface charge map for the two lowest odd SPs. (b) Normalized coupling constant squared for even and odd modes versus l for z_E : 1.2 nm (b), 2.4 nm (c), and 4 nm (d).

The SP resonant frequencies in Eq. (2) have the form

$$\omega_{l,\sigma} = \frac{\omega_p}{\sqrt{\epsilon_\infty + \epsilon_D \frac{\xi_l + \sigma}{\xi_l - \sigma}}}, \quad (3)$$

with $\xi_l = [(3R + \delta - z_0)(R + \delta - z_0)/(R - z_0)(R + z_0)]^{l+1/2}$. Note that, for simplicity, we focus here in the case $R_{1,2} = R$, but general expressions can be found in the SM. Importantly, for large l , $\xi_l \gg 1$, which enables us to write $\omega_{ps} \sim (\omega_p / \sqrt{\epsilon_\infty + \epsilon_D})$. The spectral overlapping giving rise to the pseudomode always peaks at a frequency slightly lower than the SP asymptotic frequency for a flat metal surface.

The coupling constants, $g_{l,\sigma}$, in Eq. (2) are mathematically involved functions of the geometric parameters of the cavity. However, without loss of generality, we can write

$$g_{l,\sigma}^2 = \frac{\mu_E^2}{\Delta^3} f\left(\frac{\Delta}{z_E + R - z_0}\right), \quad (4)$$

where $f(\cdot)$ contains all the dependence on the emitter position and $\Delta = (R + \delta - z_0)(3R + \delta - z_0)/(2R + \delta - z_0)$

gives the inverse volume scaling of $J(\omega)$ anticipated in Fig. 1. Equation (4) proves formally that the cavity performance can be improved by reducing its overall size, as this increases the coupling strength for all SP modes. Let us remark that the analytical decomposition of $J(\omega)$ given by Eqs. (2)–(4) proves the suitability of TO for the description of quantum nano-optical phenomena. It provides naturally a convenient and efficient quantization of EM fields in lossy, complex nanocavities, a research area of much theoretical activity lately [31,32].

In the following, we test our analytical approach. Figure 4(a) plots $J(\omega)$ for the case $z_E = 0.3\delta$ in Fig. 3(c). Red dashed-dotted and black dashed lines plot exact TO and EM calculations, respectively. The spectrum obtained from Eq. (2) is rendered as the green solid line. It reproduces $J(\omega)$ satisfactorily except for a small red-shift in the lowest frequency peak (with respect to the exact TO prediction). The various contributions to $J(\omega)$ in Eq. (2) are plotted in blue dashed and solid orange lines in Fig. 3(a). These two sets correspond to even ($\sigma = +1$) and odd ($\sigma = -1$) SP modes, respectively. Note that the former (latter) blue-shifts (red-shifts) towards ω_{ps} for increasing l . These different trends originate from the ratio $(\xi_l + \sigma)/(\xi_l - \sigma)$ in the denominator of Eq. (4), which is always larger (smaller) than 1 for $\sigma = +1$ ($\sigma = -1$). The insets of Fig. 4(a) depict induced surface charge density maps for the maxima corresponding to the two lowest odd SP contributions. Note that due to their antisymmetric character, these are purely dark, dipole-inactive, modes in the quasistatic limit.

Figures 4(b)–(d) plot Eq. (4) for both SP symmetries as a function of the mode index l and evaluated at the three z_E 's in Fig. 3(c). For QEs in close proximity to one of the particles ($z_E = 0.15\delta$), $g_{l,\pm 1}^2$ are largest. The coupling strength dependence on l is very similar for both mode symmetries and peaks at $l \approx 12$. This indicates that high multipolar dark SPs are responsible for the main contributions to $J(\omega)$. At intermediate positions, $z_E = 0.3\delta$, both coupling constants decrease, being the reduction much more pronounced in $g_{l,-1}^2$. Finally, $g_{l,-1}^2$ vanishes at the cavity center ($z_E = 0.5\delta$), and the QE interacts only with even SPs having $l \sim 3$. The bright character of these plasmon resonances translates into an increase of radiative losses, which worsens significantly the cavity performance. Figures 4(b)–(d) evidence that the remarkable (several orders of magnitude) enhancement in $J(\omega_{ps})$ shown in Fig. 3(b) for z_E away from the $\delta/2$ is caused by two different mechanisms. On the one hand, the emitter interacts more strongly with even SPs (of increasing multipolar order). On the other hand, it can couple to a whole new set of dark modes contributing to $J(\omega)$, those with odd symmetry, which are completely inaccessible for $z_E = \delta/2$. It is the combination of these two effects which makes possible for one to realize plasmon-exciton strong coupling in nanocavities with $\delta \sim 5 - 10$ nm.

Finally, in order to prove the predictive value of our analytical method, we calculate the plasmon-exciton coupling strength for geometrical and material parameters modeling the experimental samples in Ref. [20] (see SM for details). Our approach predicts $g_{0,+1} = 19$ meV for the dipolar SP mode, and $g_{PS}^{\text{eff}} = 120$ meV for the pseudomode. The latter is in good agreement with the measured value: $g_{\text{exp}} = 90$ meV. This indicates that, in accordance with our theoretical findings, high order multipolar dark modes seem to play a relevant role in the QE-SP interactions taking place in the nanocavity samples that lead to single molecule strong coupling.

In conclusion, we have presented a transformation optics description of plasmon-exciton interactions in nanometric gap cavities. We have shown that it is the dark pseudomode that builds up from the spectral overlapping of high frequency plasmonic modes which governs the energy exchange between emitter and cavity field. The quasianalytical character of our approach allows for a thorough exploration of these hybrid systems, revealing that the coupling can be greatly enhanced when the emitter is displaced across the gap. We have obtained analytical expressions that prove that this increase of the spectral density in asymmetric positions is caused by not only even, but also odd modes. Finally, we have verified the predictive value of our analytical approach against recent experimental data, which demonstrates its validity as a design tool for nanocavities sustaining plasmon-exciton-polaritons at the single emitter level.

This work has been funded by the EU Seventh Framework Programme under Grant Agreement No. FP7-PEOPLE-2013-CIG-630996, the European Research Council (ERC-2011-AdG Proposal No. 290981), and the Spanish MINECO under Contracts No. MAT2014-53432-C5-5-R and No. FIS2015-64951-R. R.-Q. L. acknowledges funding by the China Scholarship Council and thanks Professor Jian-Chun Cheng for guidance and support.

*a.fernandez-domínguez@uam.es

†fj.garcia@uam.es

- [1] D. E. Chang, A. S. Sorensen, P. R. Hemmer, and M. D. Lukin, *Phys. Rev. Lett.* **97**, 053002 (2006).
- [2] P. Törmä and W. L. Barnes, *Rep. Prog. Phys.* **78**, 013901 (2015).
- [3] M. S. Tame, K. R. McEnery, S. K. Özdemir, J. Lee, S. A. Maier, and M. S. Kim, *Nat. Phys.* **9**, 329 (2013).
- [4] A. González-Tudela, P. A. Huidobro, L. Martín-Moreno, C. Tejedor, and F. J. García-Vidal, *Phys. Rev. B* **89**, 041402(R) (2014).
- [5] A. Trügler and U. Hohenester, *Phys. Rev. B* **77**, 115403 (2008).
- [6] E. Waks and D. Sridharan, *Phys. Rev. A* **82**, 043845 (2010).
- [7] S. Savasta, R. Saija, A. Ridolfo, O. Di Stefano, P. Denti, and F. Borghese, *ACS Nano* **4**, 6369 (2010).
- [8] A. Manjavacas, F. J. García de Abajo, and P. Nordlander, *Nano Lett.* **11**, 2318 (2011).
- [9] R. Esteban, J. Aizpurua, and G. W. Bryant, *New J. Phys.* **16**, 013052 (2014).
- [10] J. Bellessa, C. Bonnand, J. C. Plenet, and J. Mugnier, *Phys. Rev. Lett.* **93**, 036404 (2004).
- [11] T. Schwartz, J. A. Hutchison, C. Genet, and T. W. Ebbesen, *Phys. Rev. Lett.* **106**, 196405 (2011).
- [12] F. Todisco, S. D'Agostino, M. Esposito, A. I. Fernández-Domínguez, M. De Giorgi, D. Ballarini, L. Dominici, I. Tarantini, M. Cuscuna, F. D. Sala, G. Gigli, and D. Sanvitto, *ACS Nano* **9**, 9691 (2015).
- [13] G. Zengin, M. Wersäll, S. Nilsson, T. J. Antosiewicz, M. Käll, and T. Shegai, *Phys. Rev. Lett.* **114**, 157401 (2015).
- [14] A. Salomon, R. J. Gordon, Y. Prior, T. Seideman, and M. Sukharev, *Phys. Rev. Lett.* **109**, 073002 (2012).
- [15] A. González-Tudela, P. A. Huidobro, L. Martín-Moreno, C. Tejedor, and F. J. García-Vidal, *Phys. Rev. Lett.* **110**, 126801 (2013).
- [16] A. Delga, J. Feist, J. Bravo-Abad, and F. J. García-Vidal, *Phys. Rev. Lett.* **112**, 253601 (2014).
- [17] S.-H. Gong, J.-H. Kim, Y.-H. Ko, C. Rodriguez, J. Shin, Y.-H. Lee, L. S. Dang, X. Zhang, and Y.-H. Cho, *Proc. Natl. Acad. Sci. U.S.A.* **112**, 5280 (2015).
- [18] T. Hartsfield, W.-S. Chang, S.-C. Yanga, T. Ma, J. Shi, L. Sun, G. Shvets, S. Link, and X. Li, *Proc. Natl. Acad. Sci. U.S.A.* **112**, 12288 (2015).
- [19] T. B. Hoang, G. M. Akselrod, and M. H. Mikkelsen, *Nano Lett.* **16**, 270 (2016).
- [20] R. Chikkaraddy, B. de Nijs, F. Benz, S. J. Barrow, O. A. Scherman, E. Rosta, A. Demetriadou, P. Fox, O. Hess, and J. J. Baumberg, *Nature (London)* **535**, 127 (2016).
- [21] L. D. Landau and E. M. Lifshitz, *Electrodynamics of Continuous Media* (Pergamon Press, Moscow, 1960).
- [22] J. B. Pendry, A. Aubry, D. Smith, and S. A. Maier, *Science* **337**, 549 (2012).
- [23] J. B. Pendry, A. I. Fernández-Domínguez, Y. Luo, and R. Zhao, *Nat. Phys.* **9**, 518 (2013).
- [24] H.-P. Breuer and F. Petruccione, *The Theory of Open Quantum Systems* (Oxford University Press, Oxford, England, 2002).
- [25] See Supplemental Material at <http://link.aps.org/supplemental/10.1103/PhysRevLett.117.107401>, which includes Refs. [26–29], for a comprehensive description of the TO theory and details of the calculations for experimental geometries.
- [26] J. B. Pendry, Y. Luo, and R. Zhao, *Science* **348**, 521 (2015).
- [27] R. Zhao, Y. Luo, A. I. Fernández-Domínguez, and J. B. Pendry, *Phys. Rev. Lett.* **111**, 033602 (2013).
- [28] L. Novotny and B. Hecht, *Principles of Nano-Optics* (Cambridge University Press, Cambridge, England, 2012).
- [29] A. Vial, A.-S. Grimault, D. Macías, D. Barchiesi, and M. Lamy de la Chapelle, *Phys. Rev. B* **71**, 085416 (2005).
- [30] I. A. Ostapenko, G. Hönig, C. Kindel, S. Rodt, A. Strittmatter, A. Hoffmann, and D. Bimberg, *Appl. Phys. Lett.* **97**, 063103 (2010).
- [31] M. B. Doost, W. Langbein, and E. A. Muljarov, *Phys. Rev. A* **90**, 013834 (2014).
- [32] P. T. Kristensen and S. Hughes, *ACS Photonics* **1**, 2 (2014).

Transformation Optics Approach to Plasmon-Exciton Strong Coupling in Nanocavities

– Supplemental Material –

Rui-Qi Li,^{1,2} D. Hernangómez-Pérez,¹ F. J. García-Vidal,^{1,3} and A. I. Fernández-Domínguez¹

¹*Departamento de Física Teórica de la Materia Condensada and Condensed Matter Physics Center (IFIMAC),
Universidad Autónoma de Madrid, E-28049 Madrid, Spain*

²*Key Laboratory of Modern Acoustics, MOE, Institute of Acoustics,*

Department of Physics, Nanjing University, Nanjing 210093, People's Republic of China

³*Donostia International Physics Center (DIPC), E-20018 Donostia/San Sebastián, Spain*

I. TRANSFORMATION OPTICS: 3D GENERALIZED INVERSION

In order to study the [quantum] dynamical properties of single quantum emitters placed in nanometric size metallic cavities supporting localized surface plasmon-polariton (SP) modes we use transformation optics, a powerful and intuitive technique successfully applied in the field of nano-optics in recent years (see recent reviews in Refs. [1]-[2]). This theoretical approach will allow us to obtain insightful analytical expressions for the spectral density and spatial profile of hybrid plasmon-exciton-polariton (PEP) modes in the quasi-static limit. As mentioned in the main text, we will assume that the electric and magnetic fields are decoupled, *i.e.* $\nabla_{\mathbf{r}} \times \mathbf{E}(\mathbf{r}) = \mathbf{0}$, since the dimer size is much smaller than the quantum emitter characteristic wavelength $\lambda_E = 2\pi c/\omega_E$. The present scheme provides as well an efficient computational framework valuable in the thorough numerical study of the quantum dynamical properties of PEPs at the single emitter level in metallic cavities with non-trivial Gaussian curvature, taking also into account the lossy character of the SP excitations.

To begin with, we consider the generalized inversion based on Ref. [3], noted as \mathcal{J} , and defined by

$$\boldsymbol{\varrho}' = \frac{R_T^2}{(z - z_0)^2 + \varrho^2} \boldsymbol{\varrho}, \quad (1a)$$

$$z' - z'_0 = -\frac{R_T^2}{(z - z_0)^2 + \varrho^2} (z - z_0). \quad (1b)$$

Here, the non-primed variables describe the original frame (with inversion point $\mathbf{z}_0 = z_0 \hat{\mathbf{z}}$), the primed variables correspond to the transformed space (with inversion point $\mathbf{z}'_0 = z'_0 \hat{\mathbf{z}}$), and R_T^2 is an arbitrary length scale. We also define $\boldsymbol{\varrho} = (x, y)$ so that $\mathbf{r} = (\boldsymbol{\varrho}, z)$ (and similarly for the primed variables). Note the additional $-$ sign in Eq. (1b) compared to the inversion transformation used in Refs. [4]-[5] which yields $z'_0 > 0$ (we fix by construction $z_0 > 0$).

Being a member of the family of inversion transformations in three-dimensional Euclidean spaces, the mapping given by Equations (1a)-(1b) transforms the infinity in a given reference frame to the inversion point in the other reference frame. It also maps a pair of metallic spheres, of radii R_1 and R_2 (see the left panel of Fig. I) into a system of two concentric spheres centered at the origin of coordinates: an inner solid sphere, of radius R'_1 , and a hollow outer sphere, of radius R'_2 (see right panel of Fig. I). The gap between the spheres in the original frame, where the quantum emitter is located (*i.e.* $R_2 \leq R_2 + z_E \leq R_2 + \delta$) is mapped within the annulus region between the transformed concentric spheres at positions far away from the inversion point.

For the transformation from the coordinate frame $\mathbf{r} \rightarrow \mathbf{r}' = \mathbf{r}'(\mathbf{r}) = \mathcal{J} \mathbf{r}$ to preserve Maxwell's equations (or, in the long wavelength limit used here, Laplace equation) the components of the dielectric permittivity tensor must necessarily verify the general relation [2]

$$\epsilon'_{\alpha', \beta'}(\mathbf{r}', \omega) = \frac{1}{\det \mathbb{J}_{\mathbf{r}'}} \sum_{\alpha, \beta} (\mathbb{J}_{\mathbf{r}'}^{-1})_{\alpha', \alpha} (\mathbb{J}_{\mathbf{r}'})_{\beta', \beta} \epsilon_{\alpha, \beta}[\mathbf{r}(\mathbf{r}'), \omega], \quad (2)$$

where $(\mathbb{J}_{\mathbf{r}'})_{\alpha, \alpha'} = \partial \mathbf{r}_{\alpha} / \partial \mathbf{r}'_{\alpha'}$ is the Jacobian matrix of the transformation. Note that Eq. (2) implies that, if in the original coordinate system the metallic spheres and the dielectric medium are spatially homogeneous, the full system becomes inhomogeneous in the transformed frame. Fortunately, this fact does not introduce additional complications in the scattering problem for the electrostatic potential $\Phi'(\mathbf{r}') = \Phi[\mathbf{r}(\mathbf{r})]$ since application of the electromagnetic (EM) boundary conditions for the Laplace equation in each region of the transformed space trivially removes any spatially dependent factor.

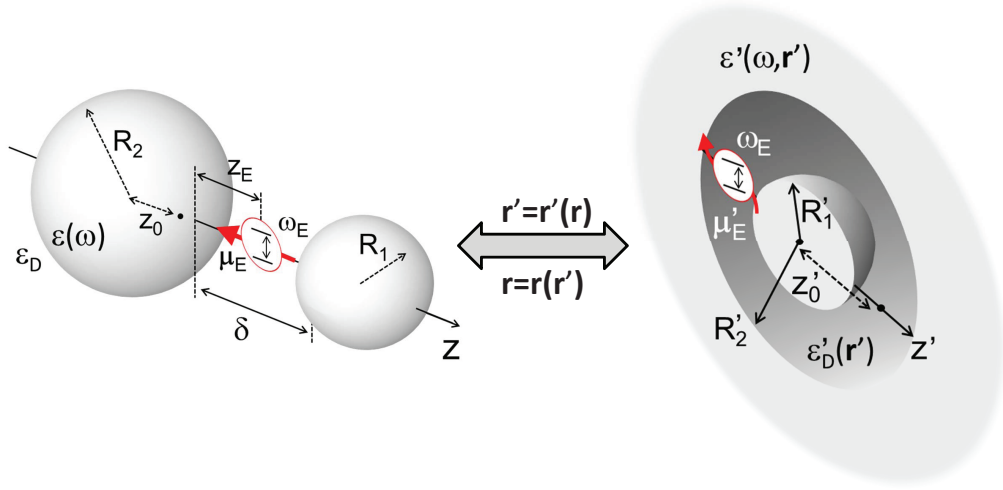


FIG. I: Sketch of the inversion transformation that maps an spherical dimer nanocavity (left) into a concentric annulus geometry (right), and vice versa. Note that the right panel shows a cross sectional view of the transformed geometry. The mapping also modifies the original permittivities, which acquire an spatial dependence in the annulus frame given by Eq. (2). The dipole source modelling the emitter is also affected by the mapping, and its primed counterpart can be expressed in the form of Eq. (3). Importantly, the transformation does not alter the spectral characteristics of the original system.

II. GENERAL SOLUTION TO THE SCATTERING PROBLEM

Our strategy to obtain the EM Green's function $\mathbb{G}(\mathbf{r}, \mathbf{r}', \omega)$, which describes the EM properties of the full system (single emitter and plasmonic metallic dimer of radii R_i , with $i \in \{1, 2\}$ and gap δ) is to take into account that the transformation given in Eqs. (1a)-(1b) is still an inversion. Then, it is well known (see Refs. [4], [5]) that the electrostatic potential has to be forcefully written as $\Phi'(\mathbf{r}') = |\mathbf{r}' - \mathbf{z}'_0| \tilde{\Phi}'(\mathbf{r}')$ where $\tilde{\Phi}'(\mathbf{r}')$ is solution of Laplace equation in the new transformed space, $\Delta_{\mathbf{r}'} \tilde{\Phi}'(\mathbf{r}') = 0$. If the source is located on the $\hat{\mathbf{z}}$ axis and oriented towards the same direction, $\boldsymbol{\mu}_E = \mu_E \hat{\mathbf{z}}$, the physical system is rotationally invariant around that axis and we can express $\tilde{\Phi}'(\mathbf{r}')$ as a sum of harmonic modes having the $\hat{\mathbf{z}}$ projection of the angular momentum $m = 0$

$$\tilde{\Phi}'(\mathbf{r}') = \sum_{l=0}^{+\infty} \left[c_l^1 \left(\frac{r'}{z'_0} \right)^l + c_l^2 \left(\frac{r'}{z'_0} \right)^{-(l+1)} \right] Y_{l,0}(\theta', \varphi') \quad (3)$$

with $\mathbf{r} = (r', \theta', \varphi')$ being the position vector expressed in spherical coordinates and $Y_{l,0}(\theta', \varphi')$ the usual spherical harmonics. From a practical point of view, the infinite series is made finite by imposing a cut-off value of the orbital angular momentum, $l \in [0, l_{\max}]$, taking into account the convergence properties of Laplace expansions. The electrostatic potential is now written as the combination of the source and scattered components, $\tilde{\Phi}'(\mathbf{r}') = \tilde{\Phi}'_s(\mathbf{r}') + \tilde{\Phi}'_{sc}(\mathbf{r}')$, and the unknown scattering coefficients in each region are obtained by means of the reflection matrix, \mathbb{R} , once the dipolar source is expanded also in harmonic modes. The latter matrix relates the scattering coefficients to the source coefficients by means of the matrix relation $\mathbf{c}^{sc} = \mathbb{R} \mathbf{c}_s$ where \mathbf{c}^{sc} and \mathbf{c}_s are block column vectors containing the coefficients of the harmonic expansion in Eq. (3).

An essential step in our approach is thus to obtain the reflection matrix, defined as $\mathbb{R} := \mathbb{T}^{-1} \mathbb{S}$, where \mathbb{T} and \mathbb{S} are, respectively, the scattering and source matrices. The latter are built from the application of the EM boundary conditions for the electric and displacement fields in the annulus frame. The scattering matrix can be written in block form

$$\mathbb{T} = \begin{pmatrix} \mathbb{T}_{11} & \mathbb{T}_{12} \\ \mathbb{T}_{21} & \mathbb{T}_{22} \end{pmatrix}, \quad (4)$$

where each of the blocks \mathbb{T}_{ij} is a tridiagonal matrix of dimension $(l_{\max} + 1) \times (l_{\max} + 1)$. In addition, it can be easily checked that for a source located in the gap, the \mathbb{S} matrix is block diagonal, $\mathbb{S} = \mathbb{S}_{ij} \delta_{i,j}$, with matrix elements related

to the \mathbb{T} matrix by means of the relation $\mathbb{S}_{ij} = -\mathbb{T}_{ij}$. The scattering matrix elements are given by

$$\begin{aligned} \mathbb{T}_{11}(l, l') &= -\delta_{l, l'} \left[(l+1)r_1'^2 + l \right] r_1'^l \\ &\quad + (2l' + 1)r_1'^{l'+1} \left[A_+(l' + 1)\delta_{l, l'+1} + A_-(l' + 1)\delta_{l, l'-1} \right], \end{aligned} \quad (5a)$$

$$\begin{aligned} \mathbb{T}_{12}(l, l') &= \delta_{l, l'} \left\{ \frac{r_1'^2 - 1}{\tilde{\epsilon}(\omega) - 1} - \left[(l+1)r_1'^2 + l \right] e^{\alpha(\omega)} \right\} r_1'^{-(l+1)} \\ &\quad + e^{\alpha(\omega)} (2l' + 1)r_1'^{-l'} \left[A_+(l' + 1)\delta_{l, l'+1} + A_-(l' + 1)\delta_{l, l'-1} \right], \end{aligned} \quad (5b)$$

$$\begin{aligned} \mathbb{T}_{21}(l, l') &= \delta_{l, l'} \left\{ \frac{r_2'^2 - 1}{\tilde{\epsilon}(\omega) - 1} - \left[l r_2'^2 + (l+1) \right] e^{\alpha(\omega)} \right\} r_2'^l \\ &\quad - e^{\alpha(\omega)} (2l' + 1)r_2'^{l'+1} \left[A_+(l' + 1)\delta_{l, l'+1} + A_-(l' + 1)\delta_{l, l'-1} \right], \end{aligned} \quad (5c)$$

$$\begin{aligned} \mathbb{T}_{22}(l, l') &= \delta_{l, l'} \left[l r_2'^2 + (l+1) \right] r_2'^{-(l+1)} \\ &\quad - (2l' + 1)r_2'^{-l'} \left[A_+(l' + 1)\delta_{l, l'+1} + A_-(l' + 1)\delta_{l, l'-1} \right]. \end{aligned} \quad (5d)$$

together with the auxiliary functions

$$A_+(l) = \sqrt{\frac{(l+1)^2}{(2l+1)(2l+3)}}, \quad (6a)$$

$$A_-(l) = \sqrt{\frac{l^2}{(2l-1)(2l+1)}}. \quad (6b)$$

Note that we have defined the reduced permittivity $\tilde{\epsilon}(\omega) := \epsilon(\omega)/\epsilon_D$ in Eqs. (5a)-(5d). This corresponds to the ratio between the permittivity of the metallic spheres, $\epsilon(\omega)$, and the permittivity of the dielectric medium in which they are embedded, ϵ_D . As mentioned in the main text, the EM response of the metal is described by means of a local Drude response function

$$\epsilon(\omega) = \epsilon_\infty - \frac{\omega_p^2}{\omega(\omega + i\gamma)}, \quad (7)$$

where ϵ_∞ is the high-frequency offset, ω_p the plasma frequency of the electron gas and Ohmic losses are taken into account through the Drude damping parameter γ (we consider silver nanospheres with $\epsilon_\infty = 4.6$, $\omega_p = 9$ eV and $\gamma = 0.1$ eV, see Ref. [9]). From the reduced permittivity, we also define the function

$$e^{\alpha(\omega)} := \frac{\tilde{\epsilon}(\omega) + 1}{\tilde{\epsilon}(\omega) - 1}. \quad (8)$$

For practical purposes, it is also convenient to express the reduced radii $r'_i = R'_i/z'_0$ for $i \in \{1, 2\}$ in terms of variables which are defined in the original frame only. After some algebra using Eqs. (1a)-(1b) we get

$$r'_1 = \frac{1 - \tilde{\Delta}_1}{1 + \tilde{\Delta}_1}, \quad (9a)$$

$$r'_2 = \frac{1 + \tilde{\Delta}_2}{1 + \tilde{\Delta}_1}, \quad (9b)$$

where

$$\tilde{\Delta}_1 := \frac{\delta + d}{2R_1 + \delta + d}, \quad (10a)$$

$$\tilde{\Delta}_2 := \frac{\delta}{d} + \frac{\delta + d}{2R_2 - d}, \quad (10b)$$

Here $d = R_2 - z_0$, and the inversion point, z_0 , is related to geometrical parameters of the spherical dimer by the relation

$$z_0 = \frac{(R_1 + R_2 + \delta)^2 + R_2^2 - R_1^2 - \sqrt{\delta(\delta + 2R_1)(\delta + 2R_2)(2R_1 + 2R_2 + \delta)}}{2(R_1 + R_2 + \delta)}. \quad (11)$$

Finally, knowledge of the scattering coefficients allows us to write the scattered electrostatic potential in the quasi-static limit and, as a consequence, the scattered electric field $\mathbf{E}^{\text{sc}}(\mathbf{r}) = \nabla_{\mathbf{r}}\Phi^{\text{sc}}(\mathbf{r}) = \nabla_{\mathbf{r}}\Phi'^{\text{sc}}[\mathbf{r}'(\mathbf{r})]$ and the corresponding EM Green's function, $\mathbb{G}^{\text{sc}}(\mathbf{r}, \mathbf{r}_E, \omega)$ defined by the general relation [6]

$$\mathbf{E}^{\text{sc}}(\mathbf{r}) = \frac{1}{\epsilon_0} \left(\frac{\omega}{c} \right)^2 \mathbb{G}^{\text{sc}}(\mathbf{r}, \mathbf{r}_E, \omega) \boldsymbol{\mu}_E, \quad (12)$$

with $\mathbf{r}_E = \underbrace{(R_2 + z_E)}_{r_E} \hat{\mathbf{z}}$ being the position of the quantum emitter measured from the origin of coordinates (center of the sphere with radius R_2 in the left panel of Fig. 1).

III. ANALYTICAL EXPRESSION FOR THE SPECTRAL DENSITY

We now present a succinct derivation of Eqs. (2)-(4) presented in the main text. The spectral density of the plasmonic gap cavity coupled to the exciton can be computed from the expression of the scattered EM Green's function evaluated at the position of quantum emitter, $\mathbb{G}^{\text{sc}}(\mathbf{r}_E, \mathbf{r}_E, \omega)$ as

$$J(\omega) = \frac{\Gamma_0(\omega)}{2\pi} \left[1 + \frac{6\pi c}{\omega} \text{Im} \mathbb{G}_{zz}^{\text{sc}}(\mathbf{r}_E, \mathbf{r}_E, \omega) \right], \quad (13)$$

where $\Gamma_0(\omega)$ is the spontaneous emission rate in vacuum at frequency ω . Going back to Eq. (12) and recalling that $\boldsymbol{\mu}_E = \mu_E \hat{\mathbf{z}}$ we easily see that the crucial step in the analytical calculation of the spectral density is the evaluation of the imaginary part of the $\hat{\mathbf{z}}$ component of the scattered electric field. In the original frame, this component is formally expressed as

$$E_z^{\text{sc}}(\mathbf{r}) = \sum_{\alpha'} [\mathbb{J}_{\mathbf{r}} \mathbb{O}_{\mathbf{r}'(\mathbf{r})}]_{z, \alpha'} E_{\alpha'}^{\text{sc}}(\mathbf{r}') \Big|_{\mathbf{r}' = \mathbf{r}'(\mathbf{r})}, \quad (14)$$

where $\mathbb{J}_{\mathbf{r}}$ has matrix elements $(\mathbb{J}_{\mathbf{r}})_{\alpha', \alpha} = \partial \mathbf{r}'_{\alpha'} / \partial \mathbf{r}_{\alpha}$ and $\mathbb{O}_{\mathbf{r}'}$ is the matrix

$$\mathbb{O}_{\mathbf{r}'} := \begin{pmatrix} \frac{x'}{r'} & \frac{x'z'}{\varrho' r'} & -\frac{y'}{\varrho'} \\ \frac{y'}{r'} & \frac{y'z'}{\varrho' r'} & \frac{x'}{\varrho'} \\ \frac{z'}{r'} & -\frac{\varrho'}{r'} & 0 \end{pmatrix}, \quad (15)$$

which still has to be transformed back to the original coordinate frame by using the inverse transformation, \mathcal{J} . Here we remind that $\mathbf{r}' = (\boldsymbol{\varrho}', z')$, $\varrho' = \sqrt{x'^2 + y'^2}$ and $r' = \sqrt{\varrho'^2 + z'^2}$.

To obtain physical insight, it is very natural to consider a *small gap approximation* for which $\delta \ll R_1, R_2$. This is obviously a limiting case but it allows to capture very well the strong coupling physics in the near and extreme near field regime. Under the assumption of small gap-to-radius ratio, it can be shown that the diagonal matrix elements belonging to the blocks \mathbb{T}_{ij} (with $i \neq j$ and $i, j \in \{1, 2\}$) present vanishing terms since $r_i'^2 - 1 \rightarrow 0$ (note that this actually takes place in the transformed frame). As a consequence, the \mathbb{R} matrix can be proved to present diagonal blocks with matrix elements

$$\mathbb{R}_{ij}(l, l') \simeq \left[\delta_{i,j} - (1 - \delta_{i,j}) e^{\alpha(\omega)} \left[\frac{1 + (i-j)\tilde{\Delta}_i}{1 + \tilde{\Delta}_1} \right]^{(i-j)(2l+1)} \right] f_l \left(\frac{1 + \tilde{\Delta}_2}{1 - \tilde{\Delta}_1}, \omega \right) \delta_{l,l'}, \quad (16)$$

and

$$f_l(r, \omega) := \frac{1}{e^{2\alpha(\omega)} r^{2l+1} - 1}. \quad (17)$$

When the relevant energies associated to the exciton are close to those of the localized surface plasmon-polariton resonances and $\gamma \ll \omega$, we can work in the so-called *high-quality resonator limit* [7] which allows us to express the spectral density as a sum of Lorentzian modes $J(\omega) \simeq \sum_{l=0}^{+\infty} \sum_{\sigma=\pm 1} J_{l,\sigma}(\omega)$ with

$$J_{l,\sigma}(\omega) = \frac{g_{l,\sigma}^2}{\pi} \frac{\gamma/2}{(\omega - \omega_{l,\sigma})^2 + (\gamma/2)^2}, \quad (18)$$

similar to the case of the planar metal surface [8] and the single sphere [9]. In the same way, all the surface plasmon-polariton resonances of the nanocavity show the same spectral width controlled by the Drude losses only. The localized surface plasmon-polariton resonant energies depend crucially on the geometrical parameters of the nanostructure, the high-frequency offset and the dielectric background properties, having the following simple functional form

$$\omega_{l,\sigma} = \frac{\omega_p}{\sqrt{\epsilon_\infty + \Omega_{l,\sigma} \epsilon_D}}, \quad (19)$$

with

$$\Omega_{l,\sigma} = \frac{\left(\frac{1 + \tilde{\Delta}_2}{1 - \tilde{\Delta}_1} \right)^{\frac{2l+1}{2}} + \sigma}{\left(\frac{1 + \tilde{\Delta}_2}{1 - \tilde{\Delta}_1} \right)^{\frac{2l+1}{2}} - \sigma}. \quad (20)$$

Importantly, the analytical results show that the exciton placed at the plasmonic gap cavity can be coupled to two different mode families: symmetric modes with resonant energies *lower* than the pseudo-mode energy, $\omega_{l,+} \lesssim \omega_{PS}$, and antisymmetric modes with resonant energies *larger* than the pseudo-mode energy, $\omega_{l,-} \gtrsim \omega_{PS}$ [see Fig. 4(a) in the main text]. Furthermore, it can be observed straightforwardly that since $r_{12} := (1 + \tilde{\Delta}_2)/(1 - \tilde{\Delta}_1) > 1$, $\Omega_{\infty,\sigma} \rightarrow 1$ for both symmetric and antisymmetric families. The convergence towards this value is very fast since the function $\Omega_{l,\sigma}$ has a power law dependence on the orbital angular momentum l . In this limit, all the resonances are localized at the surface plasmon-polariton asymptotic frequency characteristic of the Drude metal

$$\omega_{\infty,\pm} = \frac{\omega_p}{\sqrt{\epsilon_\infty + \epsilon_D}}, \quad (21)$$

the latter being roughly equal to the pseudomode frequency $\omega_{PS} \lesssim \omega_\infty$ for very small gaps.

The coherent coupling factors $g_{l,\sigma}^2 = g_{l,\sigma}^2(\mu_E, z_E, R_1, R_2, \delta)$ between the exciton and the localized surface plasmon-polaritons can be expressed in compact form as

$$g_{l,\sigma}^2 = \frac{\mu_E^2 \omega_p}{4\pi \epsilon_0 \hbar \Delta^3} \left(\frac{\omega_{l,\sigma}}{\omega_p} \right)^3 \frac{\sigma}{2} \frac{\zeta^4}{1 - \zeta} \eta_{l,\sigma}^+ \chi_l(-\zeta) \chi_{l+1}(\zeta) \left[1 + \mathcal{C}_{l,\sigma}(\zeta, \tilde{\Delta}_1, \tilde{\Delta}_2) \right], \quad (22)$$

with

$$\mathcal{C}_{l,\sigma}(\zeta, \tilde{\Delta}_1, \tilde{\Delta}_2) := \frac{1}{2} \frac{\eta_{l,\sigma}^-}{\eta_{l,\sigma}^+} \left[\left(\frac{1 - \tilde{\Delta}_1}{1 + \tilde{\Delta}_1} \right)^{-(2l+1)} |1 - \zeta|^{2l+1} \frac{\chi_l(-\zeta)}{\chi_{l+1}(\zeta)} + \left(\frac{1 + \tilde{\Delta}_2}{1 + \tilde{\Delta}_1} \right)^{2l+1} |1 - \zeta|^{-(2l+1)} \frac{\chi_{l+1}(\zeta)}{\chi_l(-\zeta)} \right]. \quad (23)$$

Here, we have defined the reduced parameters

$$\chi_l(\zeta) := 1 + \frac{l\zeta}{1 - \zeta}, \quad (24a)$$

$$\zeta := \frac{\Delta}{r_E - z_0}, \quad (24b)$$

$$\eta_{l,\sigma}^\pm := \frac{(1 \pm 1) \left(\frac{1 + \tilde{\Delta}_2}{1 - \tilde{\Delta}_1} \right)^{\frac{2l+1}{2}} - \sigma(1 \mp 1)}{\left[\left(\frac{1 + \tilde{\Delta}_2}{1 - \tilde{\Delta}_1} \right)^{\frac{2l+1}{2}} - \sigma \right]^2}, \quad (24c)$$

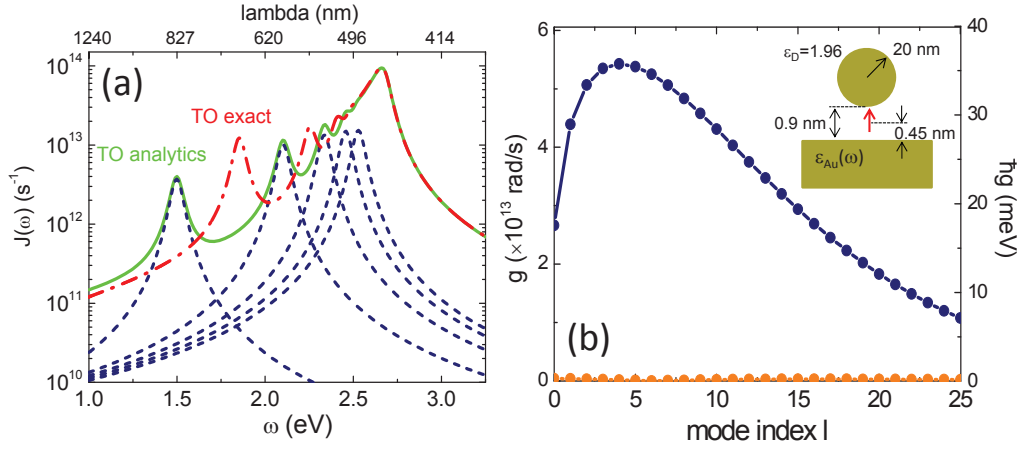


FIG. II: (a) TO exact (red dashed-dotted line) and analytical (green solid line) spectral density for the geometry modelling the experimental samples in Ref. 10 [see inset of panel (a)]. Dark blue dashed lines plot the 5 lowest terms in the Lorentzian decomposition of the analytical $J(\omega)$. (b) Coupling constants for the various even (dark blue) and odd (orange) SP modes contributing to the spectral density in panel(a). As expected (see main text), the contribution due to odd modes is negligible.

and introduced the length governing the volume scaling of the spectral density

$$\Delta := \frac{2(\delta + d)}{1 + \tilde{\Delta}_1}. \quad (25)$$

The structure of the coherent coupling factors given in Eq. (22) admits the following interpretation. The first part is associated with the diagonal blocks of the reflection matrix, $\mathbb{R}_{ij}\delta_{ij}$. As such, we can interpret this term as being the contribution to the scattered field from the two independent spheres. The term $\mathcal{C}_{l,\sigma}(\zeta, \tilde{\Delta}_1, \tilde{\Delta}_2)$ is a consequence of the non-trivial off-diagonal blocks in the reflection matrix, $\mathbb{R}_{ij}(1 - \delta_{ij})$. Therefore, it describes a *cooperative effect* between the two nanospheres due to the presence of the quantum emitter, which manifests in the spectral density. To support this interpretation, we note that both contributions have necessarily to vanish for $l \rightarrow +\infty$, $\eta_{\infty,\sigma}^{\pm} \rightarrow 0$ (essentially, for convergence reasons). However, the $-$ term, $\eta_{l \rightarrow +\infty,\sigma}^{-} \sim r_{12}^{-l}$, vanishes much faster than the $+$ term, $\eta_{l \rightarrow +\infty,\sigma}^{+} \sim 2r_{12}^{-l/2}$. Since for higher orbital angular momenta only the strongly localized SPs survive, the contribution due to $\mathcal{C}_{l,\sigma}(\zeta, \tilde{\Delta}_1, \tilde{\Delta}_2)$ has to represent the plasmonic hybridization across the gap of the nanocavity.

IV. COUPLING STRENGTH CALCULATION FOR NATURE 535, 127 (2016)

In this section, we apply our TO approach for the calculation of the exciton-plasmon coupling strength corresponding to the different SP modes supported for the experimental sample in Ref. 10. Mimicking the experimental conditions, we consider a sphere with $R_2 = 20 \text{ nm}$ separated from a flat surface ($R_1 \gg R_2$) by a $\delta = 0.9 \text{ nm}$ gap. The background permittivity is set to $\epsilon_D = 1.96$, and the gold permittivity is described through a Drude model with $\epsilon_{\infty} = 9.7$, $\omega_p = 8.91 \text{ eV}$ and $\gamma = 0.08 \text{ eV}$ (parameters taken from Ref. [11]). The QE, placed at the gap center, is modelled through a dipole source with $\mu_E = 3.8 \text{ D} = 0.079 \text{ e} \cdot \text{nm}$. Note that μ_E^2/R_2^3 , z_E/δ and δ/R_2 (all magnitudes that play a key role in $J(\omega)$, see main text) are very similar to those considered in Figure 4(d).

Figure II(a) plots the spectral density for the system above, obtained from both exact (red dashed-dotted line) and analytical (green solid line) TO calculations. The 5 lowest terms in the Lorentzian decomposition of the latter are also shown in dark blue dashed lines. Note that these correspond to even modes (due to the central position of the emitter, the contribution of odd SPs to $J(\omega)$ is negligible, see main text). The exact TO spectrum overlaps with $J(\omega)$ obtained from full EM simulations (not shown here). This is due to the fact that, contrary to the cavity considered in Figure 4 of the main text, the quasi-static approximation is very accurate for the experimental (nanometric-sized) geometry in Ref. [10]. The spectral density presents a dipolar SP maximum at 1.85 eV (670 nm), in very good agreement with experiments, 665 nm . Our calculations yield a Purcell factor equal to $4.3 \cdot 10^6$ for this SP resonance, a value which is also in accordance with measurements ($3.5 \cdot 10^6$). As discussed in the main text, the small gap approximation inherent to our analytical TO approach, leads to red-shifted spectral density maxima at low frequencies. Thus, the analytical dipole SP peak in Figure II(a) emerges at 1.5 eV (827 nm), and the corresponding Purcell enhancement is $3 \cdot 10^6$.

Figure II(b) renders the coupling constants, $g_{l,\sigma}$, versus mode index l , for the different SP modes contributing to the spectra in panel (a). Even and odd modes are rendered in dark blue and orange dots, respectively. As anticipated, the coupling strength for odd SPs is negligible. Note that the coupling constants are obtained for the analytical $J(\omega)$. For the lowest, dipolar, SP mode, we obtain $g_{0,+1} = 19$ meV. A Lorentzian fitting to the corresponding maxima for exact calculations yields $g_{\text{dip}}^{\text{fit}} = 36$ meV. The difference between these two theoretical results (~ 20 meV) originates from the inherent inaccuracy of the analytical approximation for the lowest SP modes [see for instance Fig. 4 (a) in the main text or Fig. II (a) in this document]. The theoretical value is still in discrepancy with the measured one, $g_{\text{exp}} = 90$ meV. In the following, we explore if we can gain insight into this deviation of our predictions from the experimental results.

Our theoretical findings (see main text) indicate that dark, higher multipolar SP modes play a key role in plasmon-exciton coupling in gap nanocavities. We can estimate the coupling strength corresponding to the pseudomode apparent in Figure II(a) at 2.65 eV (470 nm). Exploiting that it results from the spectral overlapping of multiple SPs, we can write [9]

$$g_{\text{PS}}^{\text{eff}} = \sqrt{\sum_{l \in \text{PS}} \sum_{\sigma=\pm 1} g_{l,\sigma}^2} = \sqrt{\sum_{l=2} g_{l,+1}^2}, \quad (26)$$

where we have dropped the vanishing contribution due to odd SPs, and we have excluded the dipole ($l = 0$) and quadrupole ($l = 1$) modes, as they give rise to clearly discernible peaks in $J(\omega)$. Equation (26) yields $g_{\text{PS}}^{\text{eff}} = 120$ meV, a prediction very similar to the result obtained from the Lorentzian fitting to the pseudomode, $g_{\text{PS}}^{\text{fit}} = 122$ meV. These two values are in much better agreement with experiments, as the discrepancy with respect to g_{exp} has been reduced by a factor of 2. This is a remarkable result, given that our theoretical approach omits experimental aspects such as the impact of inter-band transitions in gold permittivity, the inhomogeneous character of the background dielectric constant, the presence of surface roughness in the nanocavity boundaries, or the uncertainty in the QE position within the gap. We believe that our findings do not only prove the predictive value of our TO-inspired theory, but they also indicate that multipolar SPs (of order higher than dipolar modes) may also have a relevant contribution to the single molecule plasmon-exciton strong coupling reported in Ref. [10].

-
- [1] J. B. Pendry, A. Aubry, D. R. Smith, and S. A. Maier, *Science* **337**, 549 (2012).
 - [2] J. B. Pendry, Y. Luo, and R. Zhao, *Science* **348**, 521 (2015).
 - [3] L. D. Landau and E. M. Lifshitz, *Electrodynamics of Continuous Media* (Pergamon Press, Moscow, 1960).
 - [4] J. B. Pendry, A. I. Fernández-Domínguez, Y. Luo, and R. Zhao, *Nat. Physics* **9**, 518 (2013).
 - [5] R. Zhao, Y. Luo, A. I. Fernández-Domínguez, and J. B. Pendry, *Phys. Rev. Lett.* **111**, 033602 (2013).
 - [6] L. Novotny and B. Hecht, *Principles of Nano-Optics* (Cambridge University Press, Cambridge 2012).
 - [7] E. Waks and D. Sridharan, *Phys. Rev. A* **82**, 043845 (2010).
 - [8] A. González-Tudela, P. A. Huidobro, L. Martín-Moreno, C. Tejedor, and F. J. García-Vidal, *Phys. Rev. B* **89**, 041402(R) (2014).
 - [9] A. Delga, J. Feist, J. Bravo-Abad, and F. J. García-Vidal, *Phys. Rev. Lett.* **112**, 253601 (2014).
 - [10] R. Chikkaraddy, B. de Nijs, F. Benz, S. J. Barrow, O. A. Scherman, E. Rosta, A. Demetriadou, P. Fox, O. Hess, and J. J. Baumberg, *Nature* **535**, 127 (2016).
 - [11] A. Vial, A.-S. Grimault, D. Macías, D. Barchiesi, and M. Lamy de la Chapelle, *Phys. Rev. B* **71**, 085416 (2005).